Density profiles near the nuclear surface of ^{44,52}Ti: An indication of α clustering

W. Horiuchi [1,2,3,4,*] and N. Itagaki [1,2,†]

[1]*Department of Physics, Osaka Metropolitan University, Osaka 558-8585, Japan*
[2]*Nambu Yoichiro Institute of Theoretical and Experimental Physics (NITEP), Osaka Metropolitan University, Osaka 558-8585, Japan*
[3]*RIKEN Nishina Center, Wako 351-0198, Japan*
[4]*Department of Physics, Hokkaido University, Sapporo 060-0810, Japan*

(Received 23 August 2022; accepted 19 October 2022; published 31 October 2022)

We investigate the degree of α (^{4}He nucleus) clustering in the ground-state density profiles of ^{44}Ti and ^{52}Ti. Two types of density distributions, shell- and cluster-model configurations, are generated fully microscopically with the antisymmetrized quasi-cluster model, which can describe both the $j-j$ coupling shell and α-cluster configurations in a single scheme. Despite both the models reproducing measured charge radius data, we found that the α clustering significantly diffuses the density profiles near the nuclear surface compared to the ideal $j-j$ coupling shell-model configuration. The effect is most significant for ^{44}Ti, while it is less for ^{52}Ti due to the occupation of the $0f_{7/2}$ orbits in the ^{48}Ca core. This difference can be detected by measuring proton-nucleus elastic scattering or the total reaction cross section on a carbon target at intermediate energies.

DOI: 10.1103/PhysRevC.106.044330

I. INTRODUCTION

Nucleon density distributions include a variety of information on the nuclear structure. Saturation of the nuclear density in the internal region and the dropoff at the nuclear surface were revealed by systematic measurements of charge density distributions using electron scattering [1]. The nucleon density distribution can also be obtained using proton-nucleus elastic scattering [2]. Such measurements were extended to unstable nuclei using the inverse kinematics [3]. Since the nuclear density is saturated in the internal region, the nuclear structure information is obtained near the nuclear surface [4,5]. For example, nuclear deformation induces a sudden enhancement of the nuclear matter radius [6–14], where the density profile near the nuclear surface is significantly diffused compared to the spherical configuration [15,16]. The nuclear "bubble" structure, the internal density depression, can also be imprinted on the nuclear surface [17].

We explore how the nuclear structure affects the density profiles near the nuclear surface. These days, exploring an α (^{4}He nucleus) cluster in medium to heavy mass nuclei has attracted attention in the context of the astrophysical interest [18]. Direct measurement of the degree of α clustering near the nuclear surface has been realized using α knockout reactions [19]. The quantification of the degree of α clustering may impact the determination of the reaction rates of astrophysically important reactions involving medium mass nuclei.

Although the clustering is exotic and intriguing to explore, the standard picture for the nuclear structure is shell structure, and the difference between these two, must appear in the density profiles near the nuclear surface. Here we choose ^{44}Ti and ^{52}Ti as representatives of medium mass nuclei. The well-developed ^{40}Ca $+\alpha$ structure of ^{44}Ti was predicted in Ref. [20]. Afterward, the inversion doublet structure was confirmed experimentally [21,22] as its supporting evidence. The α-cluster structure of ^{44}Ti was microscopically investigated [23]. Establishing the degree of the clustering in ^{44}Ti may impact the ^{40}Ca$(\alpha,\gamma)^{44}$Ti reaction rate [24]. The influence of the α clustering on the reaction rate was discussed for ^{48}Ti using the $(p, p\alpha)$ knockout reactions [25]. We remark that the mechanism of the emergence of the α cluster near the nuclear surface in medium mass nuclei was recently suggested concerning the tensor force [26].

In this paper, we discuss the difference of the density profiles near the nuclear surface between cluster and shell models by taking an example of ^{44}Ti. We also examine the case of ^{52}Ti to clarify the role of excess neutrons. The study along this line may give a hint for the research into the emergent mechanism of α particles in the neutron-rich nuclei toward understanding nuclear matter properties. For this purpose, we need a model that can describe both the shell and cluster configurations in a single scheme. Here we employ the antisymmetrized quasi-cluster model (AQCM [27–40]). This model allows one to smoothly transform the cluster-model wave function to the $j-j$ coupling shell one, and these two can be treated on the same footing.

The paper is organized as follows. Section II summarizes the present approach to investigate the α clustering in the density profiles of ^{44}Ti and ^{52}Ti. How to calculate the density distributions that have shell and cluster configurations using the AQCM is explained in Sec. II A. For the sake of convenience, some definitions of the nuclear radii are given

*whoriuchi@omu.ac.jp
†itagaki@omu.ac.jp

in Sec. II B. To connect obtained density profiles with reaction observables, a high-energy reaction theory, the Glauber model, is briefly explained in Sec. II C. Section III presents our results. First, in Sec. III A, we discuss the properties of the wave functions with the shell and cluster configurations. Definitions and characteristics of the two types of model wave functions are described in detail. In Sec. III B, we compare the resulting density profiles and discuss the relationship between these density profiles and reaction observables. Section III C clarifies the difference in the shell- and cluster-model approaches in the density profiles. Finally, the conclusion is given in Sec. IV.

II. METHODS

A. Density distribution with antisymmetrized quasi-cluster model (AQCM)

The AQCM ansatz of the core (^{40}Ca or ^{48}Ca) plus α particle wave function, which can be transformed to the $j-j$ coupling shell model one, is defined by the fully antisymmetric ($\mathcal{A}$) product of the core and α wave functions as

$$\Phi(\nu_{\rm C}, \nu_\alpha, R, \Lambda_p, \Lambda_n) = \mathcal{A}\{\Phi_{\rm C}(\nu_{\rm C})\Phi_\alpha(\nu_\alpha, R, \Lambda_p, \Lambda_n)\}. \quad (1)$$

The wave function of the core nucleus Φ_C with the oscillator size parameter ν_C is constructed based on the multi-α cluster model [41]. For ^{40}Ca, the core wave function is obtained by taking small distances among ten α clusters; this nucleus corresponds to the closure of the *sd* shell and the shell- and cluster-model wave functions coincide at the zero-distance limit of the intercluster distances. For ^{48}Ca, we need to put additional eight neutrons describing the neutron number $N = 28$ subclosure of the $0f_{7/2}$ shell, and AQCM allows a simple description to transform the cluster model to the shell model. The details are given in Ref. [32].

The wave function of the α particle at the distance between the center-of-mass coordinate of the core and the α particle, R, is defined as the product of the single-particle Gaussian wave packet as

$$\Phi_\alpha(\nu, R, \Lambda_p, \Lambda_n) = \phi_1^\nu(\uparrow, p)\phi_2^\nu(\downarrow, p)\phi_3^\nu(\uparrow, n)\phi_4^\nu(\downarrow, n) \quad (2)$$

with a single-nucleon Gaussian wave packet with spin χ_s ($s = \uparrow$ or $\downarrow$) and isospin η_t ($t = p$ or n) wave functions

$$\phi_i^\nu(s, t) = \left(\frac{2\nu}{\pi}\right)^{3/4} \exp[-\nu(\boldsymbol{r}_i - \boldsymbol{\zeta}_t)^2]\chi_s\eta_t, \quad (3)$$

where

$$\boldsymbol{\zeta}_t = \boldsymbol{R} + i\Lambda_t \boldsymbol{e}_t^{\rm spin} \times \boldsymbol{R} \quad (4)$$

with $\boldsymbol{e}_t^{\rm spin}$ being a unit vector for the intrinsic-spin orientation of a nucleon. Note that it corresponds to the ordinary Brink α-cluster wave function in Ref. [41] by taking $\Lambda_t = 0$. A limit of $R \to 0$ leads to the SU(3) limit of the shell-model configuration. The $j-j$ coupling shell-model wave function can be expressed by introducing $\Lambda_t = 1$ with $R \to 0$ [30]. For example, in ^{44}Ti, the α cluster is changed into $(0f_{7/2})^4$ configuration using AQCM. Thus, the model wave function can describe both the shell and α-cluster configurations in a single scheme.

Finally, the density distribution in the laboratory frame is obtained by averaging the intrinsic density distribution over angles as

$$\rho_t(r) = \frac{1}{4\pi}\int d\hat{\boldsymbol{r}}\, \rho_t^{\rm int}(\boldsymbol{r}), \quad (5)$$

where $\rho_t^{\rm int}$ is obtained by using the Slater determinant of ^{44}Ti or ^{52}Ti represented as Φ

$$\rho_t^{\rm int}(\boldsymbol{r}) = \langle\Phi|\sum_{i\in t}\delta(\boldsymbol{r}_i - \boldsymbol{r})|\Phi\rangle/\langle\Phi|\Phi\rangle, \quad (6)$$

where the summation is taken over protons ($t = p$) or neutrons ($t = n$). Note that $\sum_{i=1}^A\langle\boldsymbol{r}_i\rangle = 0$ is imposed and the center-of-mass motion is ignored as the mass number $A \approx 40$–50 is large.

B. Definitions of radii

The root-mean-square (rms) point-proton, neutron, and matter radii are calculated by

$$r_p = \sqrt{\frac{4\pi}{Z}\int_0^\infty dr\, r^4\rho_p(r)}, \quad (7)$$

$$r_n = \sqrt{\frac{4\pi}{N}\int_0^\infty dr\, r^4\rho_n(r)}, \quad (8)$$

$$r_m = \sqrt{\frac{4\pi}{A}\int_0^\infty dr\, r^4[\rho_p(r) + \rho_n(r)]}, \quad (9)$$

where Z denotes the proton number. The charge radius $r_{\rm ch}$ is converted from the theoretical point-proton radius r_p by using the formula [42,43]

$$r_{\rm ch}^2 = r_p^2 + r_{{\rm ch},p}^2 + \frac{N}{Z}r_{{\rm ch},n}^2 + \frac{3\hbar^2}{4m_p^2c^2}, \quad (10)$$

where $r_{{\rm ch},t}^2$ is the second moment of the nucleon charge distribution, and the fourth term of Eq. (10) is the so-called Darwin-Foldy term, which comes from relativistic correction.

C. Reaction observables within the Glauber model

Proton-nucleus elastic scattering at intermediate energy is one of the most direct ways to extract the density profiles near the nuclear surface. We remark that the whole density distribution can be obtained by measuring up to backward angles [44,45], although the internal density has large uncertainties. As long as the nuclear surface density is of interest, only cross sections at forward angles—to be more specific, the cross section at the first peak in proton-nucleus diffraction—is needed to extract the "diffuseness" of the density distribution as prescribed in Ref. [15]. To connect the density profile with reaction observables at intermediate energies, we employ a high-energy microscopic reaction theory, the Glauber model [46].

The elastic scattering differential cross section is evaluated by

$$\frac{d\sigma}{d\Omega} = |f(\theta)|^2 \quad (11)$$

with the scattering amplitude of the proton-nucleus elastic scattering [47]

$$f(\theta) = F_C(\theta) + \frac{ik}{2\pi}\int d\boldsymbol{b}\, e^{-i\boldsymbol{q}\cdot\boldsymbol{b}+2i\eta\ln(kb)}(1-e^{i\chi_{pT}(\boldsymbol{b})}), \quad (12)$$

where $F_C(\theta)$ is the Rutherford scattering amplitude, $\boldsymbol{b}$ is the impact parameter vector, and η is the Sommerfeld parameter. The relativistic kinematics is used for the wave number k.

The optical phase-shift function χ_{pT} includes all dynamical information in the Glauber model, but its evaluation involves multifold integrations. For practical calculations, the optical-limit approximation (OLA) [46,47] is made to compute the optical phase-shift function as

$$i\chi_{pT}(\boldsymbol{b}) \approx -\int d\boldsymbol{r}\,[\rho_p(\boldsymbol{r})\Gamma_{pp}(\boldsymbol{b}+\boldsymbol{s}) + \rho_n(\boldsymbol{r})\Gamma_{np}(\boldsymbol{b}+\boldsymbol{s})], \quad (13)$$

where $\boldsymbol{r} = (\boldsymbol{s}, z)$ with z being the beam direction. The inputs to the theory are the projectile's density distributions and proton-proton (neutron-proton) profile function Γ_{pp} (Γ_{np}). The parametrization of the profile function is given in Ref. [48]. Once all the inputs are set, the theory has no adjustable parameter, and thus the resulting reaction observables must reflect the density profiles of the projectile nucleus. The OLA works well for proton-nucleus scattering as demonstrated, e.g., in Refs. [49,50], and its accuracy compared to those obtained by the full evaluation of the optical phase-shift function were discussed in Refs. [50–53].

The density profile can also be reflected in the total reaction cross sections at medium to high incident energies, which are a standard physical quantity to investigate the nuclear size properties. Here, we investigate the total reaction cross sections on a carbon target, as a carbon target is superior to a proton target to probe the density distributions near the nuclear surface [54,55]. In the Glauber model [46], the cross section is calculated as

$$\sigma_R = \int d\boldsymbol{b}\,(1-|e^{i\chi_{PT}(\boldsymbol{b})}|^2). \quad (14)$$

Since the multiple scattering effects cannot be neglected in the nucleus-nucleus collision, the nucleon-target formalism in the Glauber model [56] is employed to evaluate projectile-target optical phase-shift function $\chi_{PT}(\boldsymbol{b})$. The inputs to the theory are the density distributions of the projectile and target and the profile function. We take harmonic-oscillator type density for the target density that reproduces the measured charge radius of ^{12}C [43]. This model works well in many examples of the nucleus-nucleus scattering involving unstable nuclei [11,13,52,53,57–59] and is a standard tool to extract nuclear size properties from the interaction cross section measurements [60–62].

III. RESULTS AND DISCUSSIONS

A. Properties of the wave functions

Here we examine two types of model wave functions: one is a shell-model-like configuration (S-type), and another is a cluster-model-like configuration (C-type). Both models reproduce the experimental charge radius data of ^{44}Ti. To clarify the role of the excess neutrons, we examine ^{52}Ti as well. Note that the charge radius of ^{52}Ti has not been measured yet, and thus we use the data of the neighboring nucleus, ^{50}Ti, 3.57 fm [43], as a reference. In the following two subsections, we explain how to construct the two model wave functions in detail.

1. Shell-model-like configuration (S-type)

The shell-model-like wave function (S-type) is practically constructed by taking the core-α distance R small with $\nu_C = \nu_\alpha = \nu$. It is known that this limit goes to the SU(3) shell-model configuration [41]. For ^{44}Ti, to express the $j-j$ coupling shell-model wave function, we take $\Lambda_p = \Lambda_n = 1$ [26], and thus the wave function of the valence nucleon orbit becomes $(0f_{7/2})_p^2(0f_{7/2})_n^2$, where p is for proton and n is for neutron. In this S-type wave function, as we fix the core-α distance small, we only have one parameter, the oscillator size parameter of ^{44}Ti, ν. This is fixed to reproduce the point-proton radius extracted from the charge radius data of ^{44}Ti. To confirm the configurations are all right, we evaluate the total harmonic oscillator quanta $\langle Q\rangle$, the expectation values of single-particle spin-orbit operators $\sum_{i=1}^A \boldsymbol{l}_i\cdot\boldsymbol{s}_i$, $\langle LS\rangle$, and single-particle parity operators $\sum_{i=1}^A P_i$ with $P_i f(\boldsymbol{r}_i) = f(-\boldsymbol{r}_i)$, $\langle P\rangle$. The last quantity represents the difference of the numbers of particles in the positive-parity orbits and negative-parity orbits. These calculated values are listed in Table I and perfectly agree with the results expected from ideal shell-model configurations: $\langle Q\rangle = 60$, $\langle LS\rangle = 0$, and $\langle P\rangle = 16$ for ^{40}Ca with the closed sd shell and 72, 6, and 12 for ^{44}Ti with the $(0f_{7/2})_p^2(0f_{7/2})_n^2$ configuration.

For ^{48}Ca, these values also agree with the ideal values of the shell model, $\langle Q\rangle = 84$, $\langle LS\rangle = 12$, and $\langle P\rangle = 8$. In the case of ^{52}Ti, as it differs from the case of ^{44}Ti, we take $\Lambda_p = 1$ and $\Lambda_n = 0.5$, resulting in the desired expectation values $\langle Q\rangle = 96$, $\langle LS\rangle = 16$, and $\langle P\rangle = 4$ for the $(0f_{7/2})_p^2(1p_{3/2})_n^2$ configuration. This is because the $0f_{7/2}$ neutron orbit is already filled by the core nucleus. The additional two neutrons are found to occupy higher j-upper orbits such as $0g_{9/2}$ when $\Lambda_n = 1$. In fact, we get $\langle Q\rangle \approx 98$ when $\Lambda_p = \Lambda_n = 1$ is taken. As the charge radius of ^{52}Ti is unknown, we also generate the ^{52}Ti wave function by extending the point-proton radius r_p by 0.05 fm, which is listed as "extended" S-type.

2. Cluster-model-like configuration (C-type)

The α-cluster-model wave function (C-type) is constructed based on the core plus α-cluster model. In this case, we take $\Lambda_p = \Lambda_n = 0$, where the four nucleons are localized at a distance R from the core nucleus. The size parameters of the core wave functions are respectively fixed to reproduce the charge radii of ^{40,48}Ca. For the C-type wave functions of ^{44,52}Ti, for the sake of simplicity, we set $\nu_C = \nu_\alpha = \nu$. This is reasonable because α-particle near the nuclear surface can be distorted by the interaction and Pauli principle from the core. In fact, the size of α-particle is somewhat enlarged compared to that in vacuum [63]. Finally, the distances between the core and α particle, R, of ^{44}Ti and ^{52}Ti are respectively fixed to reproduce their charge radii. Hereafter we refer to this model as C-type.

TABLE I. Properties of the shell-model-like (S-type) and α-cluster-model-like (C-type) wave functions. Values in parentheses are obtained with ideal configurations.

	ν (fm^{-2})	R (fm)	Λ_p	Λ_n	$\langle Q\rangle$	$\langle LS\rangle$	$\langle P\rangle$	$r_{\rm ch}$ (fm)
^{40}Ca	0.1315				60.0 (60)	0.0 (0)	16.0 (16)	3.478
^{44}Ti (S-type)	0.1270	0.20	1	1	72.0 (72)	6.0 (6)	12.0 (12)	3.611
^{44}Ti (C-type)	0.1315	2.85	0	0	72.9	0.0 (0)	13.2	3.611
^{48}Ca	0.1311				84.2 (84)	12.0 (12)	8.4 (8)	3.476
^{52}Ti (S-type)	0.1297	0.20	1	0.5	96.2 (96)	15.5 (16)	4.4 (4)	3.569
^{52}Ti (C-type)	0.1311	1.60	0	0	96.5	11.2	4.9	3.569
^{52}Ti (extended, S-type)	0.1260	0.20	1	0.5	96.2 (96)	15.5 (16)	4.4 (4)	3.619
^{52}Ti (extended, C-type)	0.1311	3.01	0	0	97.4	11.4	5.9	3.619

Table I also lists the properties of the C-type wave functions. For ^{44}Ti, the $\langle LS\rangle$ values are zero as $\Lambda_p = \Lambda_n = 0$. The core and cluster distance is determined to be $R = 2.85$ fm, implying well-developed α clustering near the nuclear surface. $\langle Q\rangle$ is a bit larger than that of the S-type. This is due to the mixing of sdg-shell orbit ($\langle Q_i\rangle = 4$, $\langle P_i\rangle = +1$), which can be confirmed from the fact that the $\langle P\rangle$ value of the C-type is larger than that of the S-type.

For ^{52}Ti, the core-α distance is found to be smaller, $R = 1.60$ fm, reproducing the charge radius of ^{50}Ti. The S-type and C-type wave functions give similar $\langle Q\rangle$ values, while $\langle LS\rangle$ value is reduced for the C-type wave function because α cluster part does not contribute to this value.

The distance becomes comparable to that of ^{44}Ti, $R \approx 3$ fm, when the extended charge radius is assumed for ^{52}Ti. In that case, increases of the $\langle Q\rangle$ and $\langle P\rangle$ values are attained by the contribution of higher shells, which is the same reason found in ^{44}Ti. The $\langle LS\rangle$ value is also reduced for the C-type compared to the S-type by the same amount, as in the case of those reproducing the charge radius of ^{50}Ti because, the S-type wave function includes $1p_{3/2}$ orbits, while the C-type wave function has no contribution from the α cluster part.

B. Density profiles and reaction observables

Here we investigate the difference between these density profiles obtained in the previous section. Table II lists the root-mean-square (rms) point-proton (r_p), neutron (r_n), and matter (r_m) radii of these density models employed in this paper. Thus far, we have obtained different density profiles that have the same charge radius, i.e., the rms point-proton radius. For ^{40}Ca and ^{44}Ti, as the numbers of protons and neutrons are the same, the rms point-neutron radius is the same as that for the protons by the definition of the AQCM ansatz of Eq. (1). For ^{52}Ti, the r_n value of the C-type is slightly smaller than that of the S-type, since an α particle is isoscalar and has no neutron-skin thickness in this model wave function. This is consistent with the results showing the negative correlations between the neutron skin thickness and α clustering [18,64].

TABLE II. Rms point-proton, neutron, and matter radii and diffuseness parameters for proton, neutron, and matter in units of fm.

	r_p	r_n	r_m	a_p	a_n	a_m
^{40}Ca	3.38	3.38	3.38	0.551	0.551	0.551
^{44}Ti (S-type)	3.51	3.51	3.51	0.557	0.557	0.557
^{44}Ti (C-type)	3.51	3.51	3.51	0.625	0.625	0.625
^{48}Ca	3.38	3.62	3.52	0.552	0.528	0.540
^{52}Ti (S-type)	3.48	3.68	3.59	0.552	0.574	0.572
^{52}Ti (C-type)	3.48	3.67	3.59	0.608	0.566	0.593
^{52}Ti (extended, S-type)	3.53	3.73	3.65	0.558	0.584	0.579
^{52}Ti (extended, C-type)	3.53	3.71	3.63	0.630	0.579	0.606

Figure 1 displays the point-proton density distributions (S-type and C-type) of ^{44}Ti. Note that the distributions are the same for the neutrons. The density distribution of ^{40}Ca is also plotted for comparison. Despite the S-type and C-type density distributions giving the same charge radii, they exhibit different density profiles. All three densities coincide at $r \approx 3$ fm, which divides the internal and outer parts of the density distribution. The internal densities are reduced in the S-type. This is attributed to the fact that, in S-type, the increase of the charge radius from ^{40}Ca to ^{44}Ti partially comes from the change of the size of the oscillator parameter, $1/\sqrt{\nu}$. This leads to the depression of the internal density. For the C-type, the internal density at around $r \approx 1$–3 fm is enhanced, which is reasonable, given that the α cluster is located at $r \approx 3$ fm. Around the surface regions, at $r \gtrsim 3$ fm, the S-type density has larger values; but the inversion occurs, and the C-type density is larger at $r \gtrsim 4$ fm.

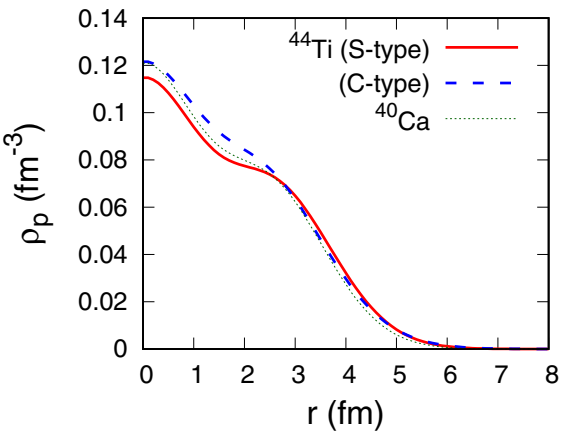

FIG. 1. Point-proton density distributions of ^{44}Ti and ^{40}Ca. The distributions are the same for the neutron.

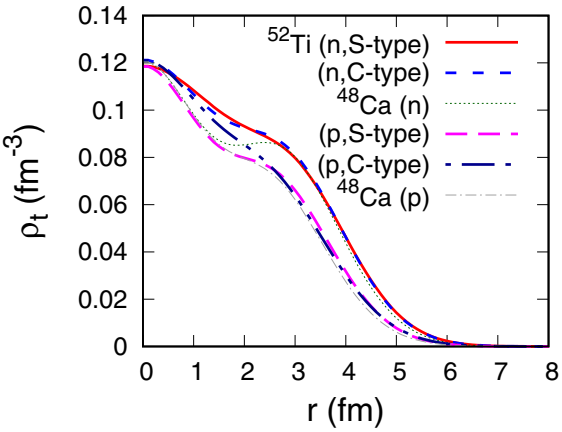

FIG. 2. Point-proton ($t = p$) and neutron ($t = n$) density distributions of ^{52}Ti and ^{48}Ca.

Figure 2 plots the point-proton and neutron density distributions of ^{52}Ti and ^{48}Ca. The charge radius of ^{50}Ti is used for ^{52}Ti to determine the parameters. While changes in the proton density distributions from ^{48}Ca to ^{52}Ti are small, they are similar to those for the ^{44}Ti case. For the neutron density distributions, though the densities at the surface region of $r \gtrsim 4$ fm are a little enhanced, the S- and C-type distributions are quite similar, implying the effect of the $(0f_{7/2})^8_n$ configuration in the ^{48}Ca part. We will address this reason in the next subsection.

These differences between the S-type and C-type are reflected in patterns of proton-nucleus diffraction. Figure 3 plots the proton-nucleus differential elastic scattering cross sections. The proton incident energies are chosen as 320 and 1000 MeV, where the experimental data of ^{40,48}Ca $+p$ are available [65–67] (crosses). Our results perfectly reproduce the data of ^{40,48}Ca $+p$ up to the second peak, which verifies our approach. For ^{44}Ti, the difference between the two types of density models (S-type and C-type) is apparent at the first and second peak positions. For a closer comparison, we plot in Fig. 4 the cross sections in a linear scale. We clearly see that the difference between the cross sections of the S-type and C-type density models is larger than the uncertainties of the experimental ^{40}Ca $+p$ cross sections at the first peak position. Measurement of these cross sections is useful to distinguish the degree of the clustering near the nuclear surface. In contrast, less difference is found in the cases of ^{52}Ti, as expected from Fig. 2. The difference is found to be comparable to the uncertainties of the experimental ^{48}Ca $+p$ cross sections. The situation is improved when we take the extended charge radius for ^{52}Ti.

These differences in the density profiles can also influence the total reaction cross sections. Here we examine the cross sections on a carbon target as they are more sensitive to the density distributions near the nuclear surface than those on a proton target [54,55]. Figure 5 displays the calculated total reaction cross sections on a carbon target as a function of the incident energy. Though the difference is not as significant as that in the proton-nucleus differential elastic scattering cross sections, the difference between the two density models (S-type and C-type) is at most about 2% for ^{44}Ti, which is larger than the present experimental precision, typically less than 1% [62,68]. The cross sections with the S- and C-type density

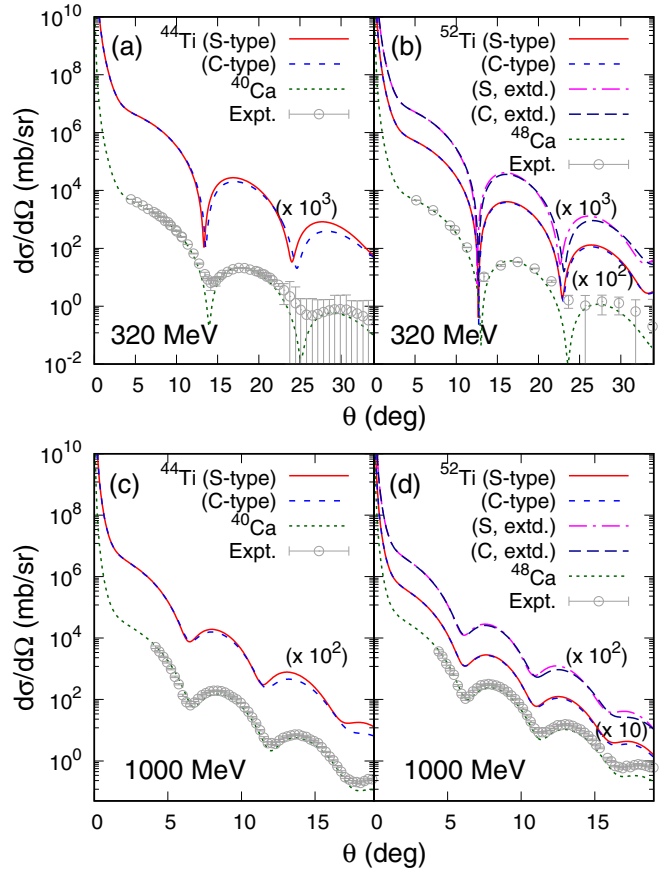

FIG. 3. Differential elastic scattering cross sections of (a), (c) ^{44}Ti $+p$ and ^{40}Ca $+p$ and (b), (d) ^{52}Ti $+p$ and ^{48}Ca $+p$ at incident energies of (a), (b) 320 MeV and (c), (d) 1000 MeV as a function of scattering angles. The experimental data are taken from Refs. [65–67]. For the sake of visibility, the cross sections of ^{44}Ti $+p$ and ^{52}Ti $+p$ are multiplied by some factors.

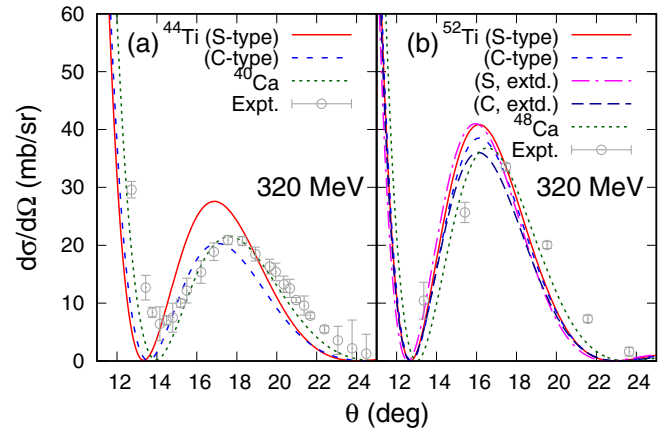

FIG. 4. Same as Figs. 3(a) and 3(b) but in a linear scale.

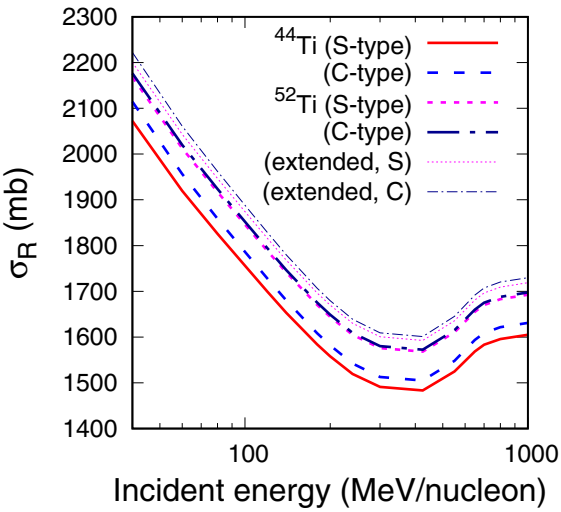

FIG. 5. Total reaction cross sections of ^{44}Ti and ^{52}Ti on a carbon target as a function of incident energy.

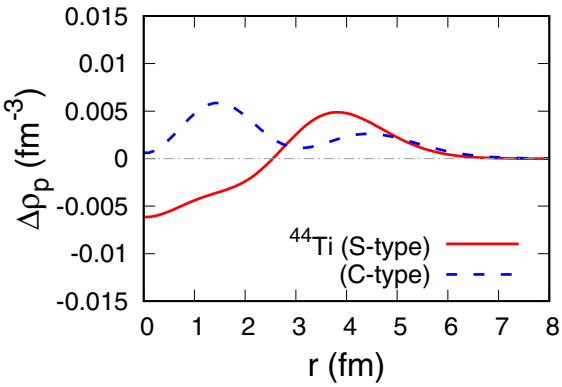

FIG. 6. Difference of point-proton density distributions between ^{44}Ti and ^{40}Ca.

distributions are almost identical for ^{52}Ti. A little difference is found when the extended charge radius is applied to ^{52}Ti.

To explore the α clustering for heavier nuclei, we investigate cases for Sn isotopes; to be more specific, ^{120}Sn $+\alpha$ and ^{132}Sn $+\alpha$. We found that The C-type configuration always gives a more diffused nuclear surface than that of S-type, as we have shown in Ti isotopes. However, the difference cannot be distinguished clearly since the density profiles of the S- and C-types become similar as the mass number increases. In such a case, a more direct way, e.g., α-knockout reaction [19], could be more useful to quantify the degree of the α clustering.

C. Close comparison of the density profiles

To clarify the origin of the differences in the density profiles, it is convenient to quantify the density profiles near the nuclear surface. For this purpose, we extract the nuclear diffuseness from the calculated density distributions using the prescription given in Ref. [15]. Nuclear diffuseness is defined in a two-parameter Fermi (2pF) function,

$$\rho_{\rm 2pF}(\bar{R}_q, a_q, r) = \frac{\rho_{0q}}{1+\exp[(r-\bar{R}_q)/a_q]}, \tag{15}$$

where the radius $\bar{R}_q$ and diffuseness a_q parameters are respectively defined for neutron ($q=n$), proton ($q=p$), and matter ($q=m$). Given the $\bar{R}_q$ and a_q values, the ρ_{0q} value is uniquely determined by the normalization condition. These parameters are determined by minimizing

$$\int_0^\infty dr\, r^2 |\rho_{\rm 2pF}(\bar{R}_q, a_q, r) - \rho_q(r)|. \tag{16}$$

Note $\rho_m = \rho_p + \rho_n$. The extracted 2pF parameters are equivalent to those obtained by fitting the first peak position and its magnitude of proton-nucleus elastic scattering [15–17].

Table II also lists the extracted diffuseness parameters for proton, neutron, and matter density distributions. These values capture well the characteristics of the density distributions. The diffuseness parameters are similar for ^{40}Ca and ^{44}Ti (S-type), while they are significantly enhanced for ^{44}Ti (C-type). In the case of ^{52}Ti, both the S- and C-types show enhanced diffuseness parameters for neutrons and matter, while for protons a behavior is found similar to that for ^{44}Ti.

To verify the reason, we plot in Fig. 6 the difference of the proton density distributions between ^{44}Ti and ^{40}Ca as a function of r, i.e., $\Delta\rho_p(r) = \rho_p(^{44}\text{Ti}, r) - \rho_p(^{40}\text{Ca}, r)$. In the S-type, the internal density is depressed, reflecting the difference of the oscillator parameters of these nuclei. It peaks at $r \approx 4$ fm, coming from the additional $(0f_{7/2})^2_p$ configuration. The $\Delta\rho_p(r)$ value of the C-type behaves quite differently, showing two peak structure that indicates the inclusion of the nodal $1p$ orbits, which significantly enhances the diffuseness of the nuclear surface [69]. The four valence nucleons mainly occupy a "sharp" $0f_{7/2}$ orbit in the S-type density, while a "diffused" $1p$ orbit is filled in the C-type density, leading to the significant difference in the density profiles near the nuclear surface.

For ^{48}Ca, the diffuseness parameter is smaller than that of ^{40}Ca as the sharp $0f_{7/2}$ neutron orbit is filled, as seen in Table II. Differently from the ^{44}Ti case, in ^{52}Ti, the neutron diffuseness is enhanced also for the S-type because the two valence neutrons are considered to occupy the $1p_{3/2}$ orbit; $0f_{7/2}$ orbits for the neutrons are fully occupied in the ^{48}Ca core. This effect leads to the enhancement of nuclear diffuseness. Figure 7 plots the differences of the proton and neutron density distributions between ^{52}Ti and ^{48}Ca. The C-type density of ^{52}Ti behaves like ^{44}Ti but the amplitudes in the internal region are larger because the resulting core-α distance is smaller than that of ^{44}Ti, as we see in Table I. We also calculate $\Delta\rho_p$ and $\Delta\rho_n$ for the extended ^{52}Ti density distributions. The enhancement of the surface region is more apparent relative to that of the internal region, and the behavior of $\Delta\rho_p$ becomes closer to that of ^{44}Ti.

In summary, the C-type density gives a more diffused surface than that of the S-type in ^{44}Ti because the cluster configuration allows the occupation of the nodal $1p$ orbit both for neutrons and protons. For ^{52}Ti, both the S- and C-types induce the enhancement of the diffuseness because the S-type also fills in the $1p_{3/2}$ orbit due to the Pauli principle from the ^{48}Ca core. The difference in the density profiles for the S-

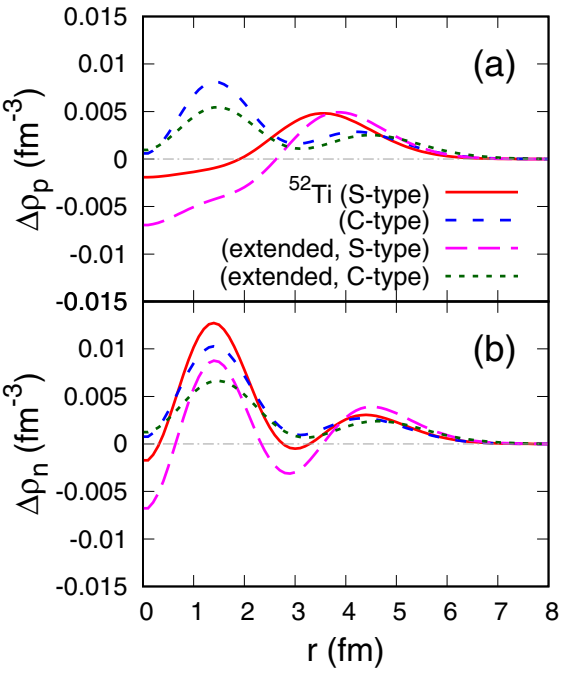

FIG. 7. Difference of the density distributions for (a) proton and (b) neutron between ^{52}Ti from ^{48}Ca.

and C-type configurations is found to be less drastic than in the case of ^{44}Ti. Investigation of the spectroscopic properties of these nuclei can corroborate this scenario, which can be achieved by using, e.g., the nucleon(s) knockout reactions [70].

IV. CONCLUSION

We have studied the degree of the α clustering in the ground state of ^{44}Ti and ^{52}Ti by using fully antisymmetrized wave functions, the antisymmetrized quasi-cluster model (AQCM), which can describe both the shell and cluster configurations in a single scheme. The characteristics of the density profiles are elucidated by assuming the shell-model and α-cluster-like configurations. The nuclear surface is diffused by nodal single-particle orbits induced by localized four nucleons at the nuclear surface. The difference between the shell and cluster configurations becomes apparent for ^{44}Ti, while it is less for ^{52}Ti because the shell-model configuration also has a diffused nuclear surface originating from the $1p_{3/2}$ orbit due to the Pauli principle between the excess neutrons.

In this paper, we show two limits of shell and cluster configurations and find that these two aspects can be distinguished by measuring the proton-nucleus elastic differential cross section up to the first peak position as well as the nucleus-nucleus total reaction cross sections. In reality, a nucleus consists of a mixture of these two limits. Thus, these measurements will tell us dominant configurations of the projectile nucleus, which offers a complementary tool to quantify the existence of α clusters near the nuclear surface.

ACKNOWLEDGMENTS

This work was in part supported by JSPS KAKENHI Grants No. 18K03635, No. 22H01214, and No. 22K03618. We acknowledge the Collaborative Research Program 2022, Information Initiative Center, Hokkaido University.

[1] R. Hofstadter, Rev. Mod. Phys. **28**, 214 (1956).
[2] H. Sakaguchi and J. Zenihiro, Prog. Part. Nucl. Phys. **97**, 1 (2017), and references therein.
[3] Y. Matsuda, H. Sakaguchi, H. Takeda, S. Terashima, J. Zenihiro, T. Kobayashi, T. Murakami, Y. Iwao, T. Ichihara, T. Suda *et al.*, Phys. Rev. C **87**, 034614 (2013).
[4] W. Horiuchi and T. Inakura, Phys. Rev. C **101**, 061301(R) (2020).
[5] W. Horiuchi and T. Inakura, Prog. Theor. Exp. Phys. **2021**, 103D02 (2021).
[6] M. Takechi, T. Ohtsubo, M. Fukuda, D. Nishimura, T. Kuboki, T. Kubo, T. Suzuki, T. Yamaguchi, A. Ozawa, T. Moriguchi, and H. Ooishi, Phys. Lett. B **707**, 357 (2012).
[7] M. Takechi, S. Suzuki, D. Nishimura, M. Fukuda, T. Ohtsubo, M. Nagashima, T. Suzuki, T. Yamaguchi, A. Ozawa, T. Moriguchi *et al.*, Phys. Rev. C **90**, 061305(R) (2014).
[8] K. Minomo, T. Sumi, M. Kimura, K. Ogata, Y. R. Shimizu, and M. Yahiro, Phys. Rev. C **84**, 034602 (2011).
[9] K. Minomo, T. Sumi, M. Kimura, K. Ogata, Y. R. Shimizu, and M. Yahiro, Phys. Rev. Lett. **108**, 052503 (2012).
[10] T. Sumi, K. Minomo, S. Tagami, M. Kimura, T. Matsumoto, K. Ogata, Y. R. Shimizu, and M. Yahiro, Phys. Rev. C **85**, 064613 (2012).
[11] W. Horiuchi, T. Inakura, T. Nakatsukasa, and Y. Suzuki, Phys. Rev. C **86**, 024614 (2012).
[12] S. Watanabe, K. Minomo, M. Shimada, S. Tagami, M. Kimura, M. Takechi, M. Fukuda, D. Nishimura, T. Suzuki, T. Matsumoto *et al.*, Phys. Rev. C **89**, 044610 (2014).
[13] W. Horiuchi, T. Inakura, T. Nakatsukasa, and Y. Suzuki, JPS Conf. Proc. **6**, 030079 (2015).
[14] W. Horiuchi, T. Inakura, and S. Michimasa, Phys. Rev. C **105**, 014316 (2022).
[15] S. Hatakeyama, W. Horiuchi, and A. Kohama, Phys. Rev. C **97**, 054607 (2018).
[16] V. Choudhary, W. Horiuchi, M. Kimura, and R. Chatterjee, Phys. Rev. C **104**, 054313 (2021).
[17] V. Choudhary, W. Horiuchi, M. Kimura, and R. Chatterjee, Phys. Rev. C **102**, 034619 (2020).
[18] S. Typel, G. Röpke, T. Klähn, D. Blaschke, and H. H. Wolter, Phys. Rev. C **81**, 015803 (2010).
[19] J. Tanaka, Z. Yang, S. Typel, S. Adachi, S. Bai, P. van Beek, D. Beaumel, Y. Fujikawa, J. Han, S. Heil *et al.*, Science **371**, 260 (2021).
[20] F. Michel, G. Reidemeister, and S. Ohkubo, Phys. Rev. Lett. **57**, 1215 (1986).
[21] T. Yamaya, S. Oh-ami, M. Fujiwara, T. Itahashi, K. Katori, M. Tosaki, S. Kato, S. Hatori, and S. Ohkubo, Phys. Rev. C **42**, 1935 (1990).
[22] T. Yamaya, K. Katori, M. Fujiwara, S. Kato, and S. Ohkubo, Prog. Theor. Phys. Suppl. **132**, 73 (1998).

[23] M. Kimura and H. Horiuchi, Nucl. Phys. A **767**, 58 (2006).
[24] H. Nassar, M. Paul, I. Ahmad, Y. Ben-Dov, J. Caggiano, S. Ghelberg, S. Goriely, J. P. Greene, M. Hass, A. Heger, A. Heinz, D. J. Henderson, R. V. F. Janssens, C. L. Jiang, Y. Kashiv, B. S. Nara Singh, A. Ofan, R. C. Pardo, T. Pennington, K. E. Rehm *et al.*, Phys. Rev. Lett. **96**, 041102 (2006).
[25] Y. Taniguchi, K. Yoshida, Y. Chiba, Y. Kanada-En'yo, M. Kimura, and K. Ogata, Phys. Rev. C **103**, L031305 (2021).
[26] C. Ishizuka, H. Takemoto, Y. Chiba, A. Ono, and N. Itagaki, Phys. Rev. C **105**, 064314 (2022).
[27] N. Itagaki, H. Masui, M. Ito, and S. Aoyama, Phys. Rev. C **71**, 064307 (2005).
[28] H. Masui and N. Itagaki, Phys. Rev. C **75**, 054309 (2007).
[29] T. Yoshida, N. Itagaki, and T. Otsuka, Phys. Rev. C **79**, 034308 (2009).
[30] N. Itagaki, J. Cseh, and M. Płoszajczak, Phys. Rev. C **83**, 014302 (2011).
[31] T. Suhara, N. Itagaki, J. Cseh, and M. Płoszajczak, Phys. Rev. C **87**, 054334 (2013).
[32] N. Itagaki, H. Matsuno, and T. Suhara, Prog. Theor. Exp. Phys. **2016**, 093D01 (2016).
[33] H. Matsuno, N. Itagaki, T. Ichikawa, Y. Yoshida, and Y. Kanada-En'yo, Prog. Theor. Exp. Phys. **2017**, 063D01 (2017).
[34] H. Matsuno and N. Itagaki, Prog. Theor. Exp. Phys. **2017**, 123D05 (2017).
[35] N. Itagaki, Phys. Rev. C **94**, 064324 (2016).
[36] N. Itagaki and A. Tohsaki, Phys. Rev. C **97**, 014307 (2018).
[37] N. Itagaki, H. Matsuno, and A. Tohsaki, Phys. Rev. C **98**, 044306 (2018).
[38] N. Itagaki, A. V. Afanasjev, and D. Ray, Phys. Rev. C **101**, 034304 (2020).
[39] N. Itagaki, T. Fukui, J. Tanaka, and Y. Kikuchi, Phys. Rev. C **102**, 024332 (2020).
[40] N. Itagaki and T. Naito, Phys. Rev. C **103**, 044303 (2021).
[41] M. Brink, in *Many-Body Description of Nuclear Structure and Reactions*, Proceedings of the International School of Physics "Enrico Fermi," Course XXXVI, edited by L. Bloch (Academic, New York, 1966), p. 247.
[42] J. L. Friar, J. Martorell, and D. W. L. Sprung, Phys. Rev. A **56**, 4579 (1997).
[43] I. Angeli and K. P. Marinova, At. Data Nucl. Data Tables **99**, 69 (2013).
[44] S. Terashima, H. Sakaguchi, H. Takeda, T. Ishikawa, M. Itoh, T. Kawabata, T. Murakami, M. Uchida, Y. Yasuda, M. Yosoi *et al.*, Phys. Rev. C **77**, 024317 (2008).
[45] J. Zenihiro, H. Sakaguchi, T. Murakami, M. Yosoi, Y. Yasuda, S. Terashima, Y. Iwao, H. Takeda, M. Itoh, H. P. Yoshida, and M. Uchida, Phys. Rev. C **82**, 044611 (2010).
[46] R. J. Glauber, *Lectures in Theoretical Physics*, edited by W. E. Brittin and L. G. Dunham (Interscience, New York, 1959), Vol. 1, p. 315.
[47] Y. Suzuki, R. G. Lovas, K. Yabana, and K. Varga, *Structure and Reactions of Light Exotic Nuclei* (Taylor & Francis, London, 2003).
[48] B. Abu-Ibrahim, W. Horiuchi, A. Kohama, and Y. Suzuki, Phys. Rev. C **77**, 034607 (2008); **80**, 029903(E) (2009); **81**, 019901(E) (2010).
[49] W. Horiuchi, S. Hatakeyama, S. Ebata, and Y. Suzuki, Phys. Rev. C **93**, 044611 (2016).
[50] S. Hatakeyama and W. Horiuchi, Nucl. Phys. A **985**, 20 (2019).
[51] K. Varga, S. C. Pieper, Y. Suzuki, and R. B. Wiringa, Phys. Rev. C **66**, 034611 (2002).
[52] B. Abu-Ibrahim, S. Iwasaki, W. Horiuchi, A. Kohama, and Y. Suzuki, J. Phys. Soc. Jpn. **78**, 044201 (2009).
[53] T. Nagahisa and W. Horiuchi, Phys. Rev. C **97**, 054614 (2018).
[54] W. Horiuchi, Y. Suzuki, and T. Inakura, Phys. Rev. C **89**, 011601(R) (2014).
[55] K. Makiguchi and W. Horiuchi, Prog. Theor. Exp. Phys. **2022**, 073D01 (2022).
[56] B. Abu-Ibrahim and Y. Suzuki, Phys. Rev. C **61**, 051601(R) (2000).
[57] W. Horiuchi and Y. Suzuki, Phys. Rev. C **74**, 034311 (2006).
[58] W. Horiuchi, Y. Suzuki, B. Abu-Ibrahim, and A. Kohama, Phys. Rev. C **75**, 044607 (2007); **76**, 039903(E) (2007).
[59] W. Horiuchi, Y. Suzuki, P. Capel, and D. Baye, Phys. Rev. C **81**, 024606 (2010).
[60] R. Kanungo, A. Prochazka, W. Horiuchi, C. Nociforo, T. Aumann, D. Boutin, D. Cortina-Gil, B. Davids, M. Diakaki, F. Farinon *et al.*, Phys. Rev. C **83**, 021302(R) (2011).
[61] R. Kanungo, A. Prochazka, M. Uchida, W. Horiuchi, G. Hagen, T. Papenbrock, C. Nociforo, T. Aumann, D. Boutin, D. Cortina-Gil *et al.*, Phys. Rev. C **84**, 061304(R) (2011).
[62] S. Bagchi, R. Kanungo, Y. K. Tanaka, H. Geissel, P. Doornenbal, W. Horiuchi, G. Hagen, T. Suzuki, N. Tsunoda, D. S. Ahn *et al.*, Phys. Rev. Lett. **124**, 222504 (2020).
[63] W. Horiuchi and Y. Suzuki, Phys. Rev. C **89**, 011304(R) (2014).
[64] Q. Zhao, Y. Suzuki, J. He, B. Zhou, and M. Kimura, Eur. Phys. J. A **57**, 157 (2021).
[65] G. D. Alkhazov, T. Bauer, R. Beurtey, A. Boudard, G. Bruge, A. Chaumeaux, P. Couvert, G. Cvijanovich, H. H. Duhm, J. M. Fontaine *et al.*, Nucl. Phys. A **274**, 443 (1976).
[66] J. J. Kelly, P. Boberg, A. E. Feldman, B. S. Flanders, M. A. Khandaker, S. D. Hyman, H. Seifert, P. Karen, B. E. Norum, P. Welch, S. Nanda, and A. Saha, Phys. Rev. C **44**, 2602 (1991).
[67] A. E. Feldman, J. J. Kelly, B. S. Flanders, M. A. Khandaker, H. Seifert, P. Boberg, S. D. Hyman, P. H. Karen, B. E. Norum, P. Welch, Q. Chen, A. D. Bacher, G. P. A. Berg, E. J. Stephenson, S. Nanda, A. Saha, A. Scott *et al.*, Phys. Rev. C **49**, 2068 (1994).
[68] M. Tanaka, M. Takechi, M. Fukuda, D. Nishimura, T. Suzuki, Y. Tanaka, T. Moriguchi, D. S. Ahn, A. Aimaganbetov, M. Amano *et al.*, Phys. Rev. Lett. **124**, 102501 (2020).
[69] W. Horiuchi, Prog. Theor. Exp. Phys. **2021**, 123D01 (2021).
[70] A. Gade and T. Glasmacher, Prog. Part. Nucl. Phys. **60**, 161 (2008) and references therein.